

A nonlinear atomization model based on a boundary layer instability mechanism

Sam S. Yoon^{a)} and Stephen D. Heister

School of Aeronautics and Astronautics, Purdue University, 315 North Grant Street, West Lafayette, Indiana 47907-1282

(Received 19 February 2003; accepted 24 September 2003; published online 3 December 2003)

An axisymmetric boundary element method has been used to simulate primary atomization of a liquid jet including the effects of the orifice passage geometry. A ring vortex is placed at the orifice exit plane; its strength and location are uniquely determined by the local boundary layer characteristics at this locale. Using this methodology, nonlinear simulations are performed that include hundreds of individual atomization events. A linear analysis due to Ponstein is used to estimate the number of droplets formed from individual rings of fluid which are pinched from the periphery of the jet. Numerous results have been obtained to assess the effects of fluid parameters and orifice design on droplet sizes and atomization characteristics. Predicted droplet sizes show agreement with some limited experimental data. © 2004 American Institute of Physics.

[DOI: 10.1063/1.1629301]

I. INTRODUCTION

The hydrodynamic instability of liquid jets has been of great interest to fluid dynamicists for more than 100 years. Despite the numerous analytical, experimental, and numerical studies over the years, high-speed jet flow is too complex to be understood completely. Unfortunately, the high-speed jet application is one of great interest because many practical devices rely on highly atomized sprays to accomplish maximum efficiency. In this case, experimental observations of the jet surface are nearly impossible as it is obscured by the droplet field surrounding the liquid core. Droplets pinched off from the liquid surface are subject to secondary atomization in higher-speed jets. In addition, collisions between one droplet and another enhance the complexities of the jet atomization process. These phenomena are greatly dependent on the initial flow condition near the nozzle exit.

Two upstream flow conditions that may affect the initial flow condition at the nozzle exit are turbulence and cavitation. While DeJuhasz¹ claimed that turbulence may be the most important factor in jet breakup process, it was later shown by Bergwerk² that the turbulence eddy viscosity in the applicable range of Reynolds numbers is not large enough to cause the disintegration of the jet. Bergwerk suspected that cavitation was the main source that produces an amplitude large enough to cause the jet breakup.

In the absence of cavitation and the substantial reduction of turbulence fluctuations through the use of a nozzle geometry promoting highly favorable pressure gradients³ atomization is still known to occur. This suggests that there are other mechanisms that contribute to the disintegration of the jet. Relaxation of the boundary layer as the fluid leaves the no-slip region inside the injector and enters a free-surface

boundary condition has long been recognized as a potential contributor to atomization. Velocity profile relaxation results in a point of inflection in the velocity profile, which is inviscidly unstable according to Rayleigh's theorem (see Schlichting⁴ and Panton⁵); vortices start to form at the point of inflection and cause a roll-up at the critical layer and eventually the instability.

Rupe⁶ observed the velocity profile relaxation has a key role in influencing the jet breakup. The boundary layer instability analysis by Shkadov⁷ predicted the unstable short wavelength of the free surface of the jet. More recently, Gordillo *et al.*⁸ performed a linear stability analysis on a coaxial jet and showed instability mechanisms due to velocity profile relaxation as being dominant over Kelvin–Helmholtz modes for all but the thinnest of boundary layers.

Many of today's atomization theories stem from the classic Kelvin–Helmholtz instability mechanism attributed to aerodynamic interactions between the liquid and gas. Reitz and Bracco⁹ observed a substantial difference in the atomization mechanism when the liquid jet was injected in different gases and Wu *et al.*¹⁰ have also reported a change in droplet size for primary atomization when a different gas density was tested for the same liquid jet.

These experiments on turbulent jets make it difficult to assess the potential contributions of underlying instabilities contributed by the boundary layer relaxation mechanism. Using a carefully manufactured orifice, Hoyt and Taylor³ were able to image this instability successfully as shown in Fig. 1(a). These researchers noted no discernable trends in this instability with changes in air velocity; a point consistent with Shkadov's theory and Gordillo *et al.*'s findings. In the presence of turbulence, the axisymmetric wave growth at the orifice exit plane may be lost; thereby providing an explanation for the lack of observation by other experimentalists, i.e., the presence of boundary layer-driven wavegrowth may

^{a)} Author to whom correspondence should be addressed. Electronic mail: ssyoon@sandia.gov

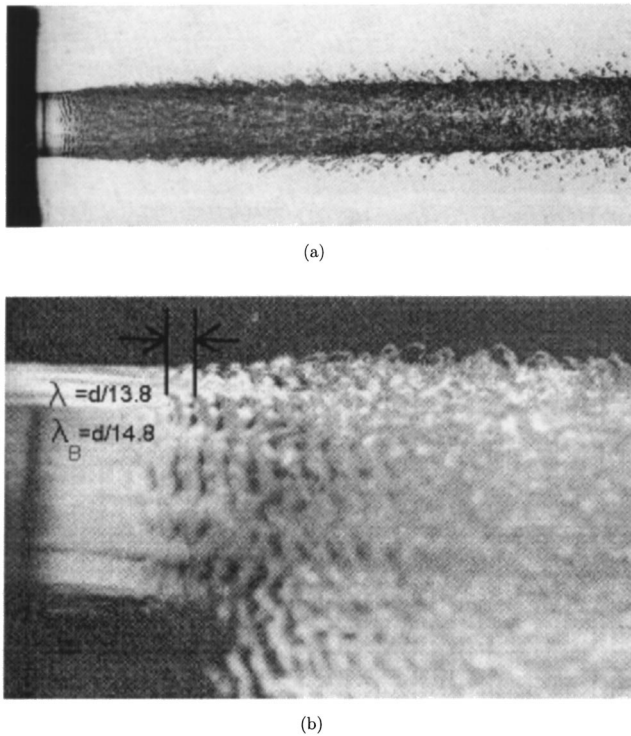


FIG. 1. (a) Typical water jet into air in the atomization regime. Experimental image by Hoyt and Taylor (Ref. 3). (b) Closeup picture shows the most dominant wavelength $\lambda_p = d/13.8$ while Brennen's theory predicts $\lambda_{p,B} = d/14.8$. Printed under the permission of the Journal of Fluid Mechanics.

not be immediately obvious and could be attributed to other mechanisms.

In a later paper by Hoyt and Taylor,¹¹ they claimed that axisymmetric waves observed in cavitating flow over bluff body show similar wavelengths to those observed in their water jet experiment. Brennen¹² had performed linear boundary layer instability analysis of Rayleigh's equation and derived the nondimensional frequency, $\gamma = 0.175$, to be the one that gives the maximum amplification at flow separation point. Using $\gamma = 0.175$ for Hoyt and Taylor's case, the theoretically predicted primary wavelength was $\lambda_p = (1/14.8)d$, where d is the orifice diameter. The experimentally observed primary wavelength was $\lambda_p = (1/13.8)d$ as shown in Fig. 1(b). The comparison between theory and experiment was very good. A recent study¹³ has shown that the aerodynamic-based linear theories tend to underpredict the wavelength for this particular condition.

Based on the evidence from these researchers, the notion that boundary layer instability is responsible for the axisymmetrically disturbed waves near nozzle exit is too compelling to ignore. For this reason, we have investigated the effect of boundary layer thickness at the nozzle exit on the liquid jet under high-speed injection conditions.

While the entire numerical method is based on the potential theory, vorticity convected from the boundary layer to the free surface can be simulated using a potential ring vortex whose effects are combined with the bulk orifice flow. This is traditionally known as superposition theory and is somewhat similar to what has been known as the "vortex-method" (see Chorin¹⁴⁻¹⁶) series of singular vortices. The

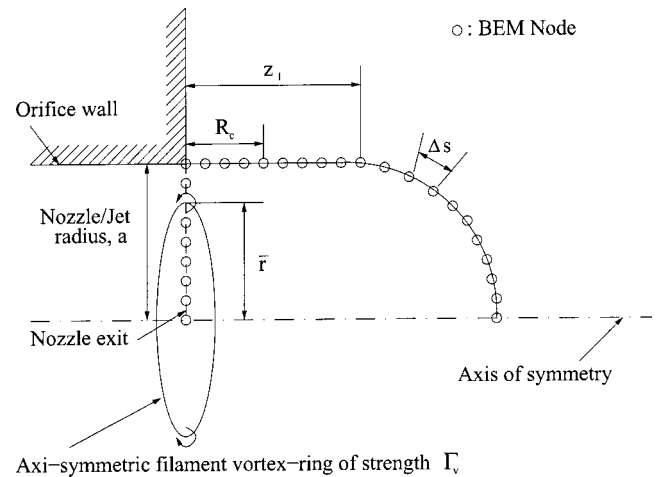


FIG. 2. Schematic of the initial jet geometry indicating computational nodes and the vortex ring used to represent the boundary layer at the orifice exit plane.

following section provides a description of the model, followed by parametric studies to address the influence of orifice length, jet speed, and Weber number on the resultant nonlinear jet evolution and droplet size characteristics.

II. MODEL ELEMENTS

The model is based on an unsteady axisymmetric potential flow of a liquid exiting a round orifice in the absence of a gas-phase medium. A bound ring vortex is utilized to simulate viscous effects associated with vorticity in the boundary layer formed in the orifice passage. Figure 2 provides a schematic representation of the geometry and appropriate nomenclature. Vortices induce motion/instability near the nozzle exit (i.e., axisymmetrically disturbed waves) and eventually cause the jet to break up into a turbulent flow. However, the flow at the nozzle exit can be nearly laminar if a highly contracted nozzle geometry induces a favorable pressure gradient.¹¹ Since the filament vortex-ring is located exactly at the nozzle exit, the computational nodes near the nozzle exit see induced velocities from the presence of the vortex ring with nodes lying the closest to the exit seeing the greatest disturbance velocities. This seems contradictory to the observed laminarized flow as shown in Fig. 1. In reality, it takes some time and distance for the rollup motion to develop and therefore the relaxation length is present regardless of the flow regime. For this reason, a cutoff for the superposition method of the filament vortex-ring is introduced using the stationary Rankine vortex model.¹⁷ The size of the Rankine vortex (i.e., R_c in Fig. 2), whose center is located at the upper corner of the nozzle exit, has little effect on droplet size and thus this is the parameter that can be set at the user's convenience. Little variation in the axial pinch-off location is observed for $R_c < 0.4$.¹⁸ We have set $R_c = 0.3$ so that the computational nodes at the near nozzle exit are not affected by the induced motion. This is essentially setting the Rankine vortex size to be the relaxation length, $R_c \approx l_r$. It should be noted that the relaxation length can be scaled with the nozzle length, l .^{6,19} A vortex ring of strength Γ_v and overall radius \bar{r}

is assumed to lie at the orifice exit plane. A computational domain represented by a simple cylindrical column of length z_l with a hemispherical cap is selected to initialize the calculation. Constant nodal spacing, Δs is employed along this domain and nodes are added as the jet issues forth from the orifice. We choose the liquid density, ρ , jet average exit velocity, U , and orifice radius, a as dimensions in the problem.

The formulation of the BEM starts with the integral representation of Laplace’s equation, $\nabla^2 \phi = 0$, with ϕ being the velocity potential. Following Liggett and Liu,²⁰ the integral form for this relation is

$$\alpha \phi(\mathbf{r}_i) + \int_{\Omega} \left[\phi \frac{\partial G}{\partial \mathbf{n}} - qG \right] d\Omega = 0, \tag{1}$$

where $\phi(\mathbf{r}_i)$ is the value of the potential at a point \mathbf{r}_i , Ω is the boundary of the 3D domain, and G is the free space Green’s function corresponding to Laplace’s equation. A second-order accurate formulation for solving Eq. (1) based on linear elements is discussed in prior works.^{21–23,18}

Contributions from the ring vortex can be obtained through the principle of superposition for potential flow. Since the Laplacian governing equation is linear, we may superpose the bulk potential flow with the potential vortex-ring:

$$\phi_t = \phi + \phi_v, \quad u_t = u + u_v, \tag{2}$$

where \mathbf{u}_v is the induced velocities due to vortex ring that can be obtained from the Biot–Savart law.^{24–26} Analytical solutions have been developed for a potential vortex ring by applying the Cauchy–Riemann equation to the stream function and by direct evaluation of the Biot–Savart law. The solutions of the stream function approach is available in the Appendix. Here $(\)_t$ represents the general or “total” solution of the jet flow. The solution of the vortex ring can be obtained by direct evaluation of Biot–Savart law.²⁶

The unsteady Bernoulli equation provides the free surface boundary condition.²⁷ This condition provides a connection between the inertial, hydrostatic, and capillary forces at the interface. Because the surface curvature, κ depends nonlinearly on the surface shape, the overall expression is nonlinear. Using the nondimensionalization described previously, the appropriate dimensionless form is

$$\frac{D\phi}{Dt} = \frac{1}{2} |u_t|^2 - \mathbf{u}_r \cdot \mathbf{u}_v - \frac{\kappa}{We} - P_g + \frac{Bo}{We} z, \tag{3}$$

where P_g is the dimensionless gas-phase pressure (assumed to be zero in the present studies), and We and Bo are the Weber and Bond numbers characterizing the flow: $We = \rho U^2 a / \sigma$ and $Bo = \rho g a^2 / \sigma$. Equation (3) is marched in time using a fourth order Runge–Kutta time integration. The curvature (κ) of the highly distorted surface is determined with full fourth-order accuracy as well.²⁸ The location of nodes on the free surface (i.e., z and r) is calculated by integrating the respective velocity components in time using the same fourth-order Runge–Kutta scheme.

Nodes are repositioned along the distorted surface using cubic splines,²⁹ and nodes can be added (due to fluid exiting the nozzle) or removed (due to atomization events) without

user intervention. The tolerance (ϵ) for the distance (d_{bi}) between the binary computational nodes is 50% of the mesh spacing (Δs). We assume the atomization event when $d_{bi} < \epsilon$. The results are insensitive to this pinch-off criteria. The current “high-speed” atomization simulation is more susceptible to numerical instability than prior low-speed atomization simulations. In the “necking” region where a droplet is pinched-off node velocities can exceed 2–7 times that of the jet speed and therefore numerical smoothing is crucial to prevent the numerical instability. We have chosen the filter function by Longuet-Higgins and Cokelet;³⁰ this filter that is designed to eliminate sawtooth point-to-point modes. The velocity potential and its normal derivative (i.e., ϕ and q) are filtered during the time integration.

The centroid of the vorticity of the viscous flow is regarded as the center of the vortex-ring. The definition of the centroid of the vorticity, weighted in the radial direction is

$$\bar{r} = \frac{\int_{r=0}^{r=1} r \omega dr}{\int_{r=0}^{r=1} \omega dr} \tag{4}$$

and the vorticity, ω , is defined as

$$\omega = \frac{\partial v}{\partial z} - \frac{\partial u}{\partial r}, \tag{5}$$

where u and v are the velocities in axial and radial direction, respectively. Assuming $\partial v / \partial z \approx 0$, i.e., parallel flow at the orifice exit plane, the centroid can be written as

$$\bar{r} = \frac{\int_{u(r=0)}^{u(r=1)} r du}{\int_{u(r=0)}^{u(r=1)} du}. \tag{6}$$

Substituting the definition of the displacement thickness, δ_1 ,³¹ into Eq. (6) and applying integration by parts give the following result:

$$\bar{r} = 1 - \delta_1. \tag{7}$$

δ_1 can be approximated using a Navier–Stokes solution of the internal flow, or appropriate analytical methods such as the Blasius solution³¹ for a flat-plate or Thwaites³² integral method.

The vortex strength Γ_v is defined as the circulation that is taken about any path enclosing the vortex-ring,

$$\Gamma_v = \oint \mathbf{u} \cdot d\mathbf{l}, \tag{8}$$

where \mathbf{u} is the internal flow velocity of the injector orifice and \mathbf{l} is the integration path. The integration is performed in the region near the orifice exit; prior studies have shown that the shear layer thins rapidly upon departure from the orifice as the boundary layer relaxes to a free-surface condition from the no-slip condition within the nozzle.²² We assume that the length of the region corresponds to a single wavelength of the disturbance. Furthermore, if we assume a purely axial flow along this region, then we can approximate the velocity on the inner surface of the region as U , the orifice exit velocity. Finally, if we assume the velocity on the upper surface is zero in connection with the no-slip boundary

condition at the start of the region, the integration of Eq. (8) gives the following dimensionless circulation for the path we have chosen:

$$\Gamma_v = \Delta z, \quad (9)$$

where Δz is the length of the region in question. We assume that this length scale is equivalent to the most unstable wavelength, λ_p , as identified by Brennen.¹² Γ_v is always positive and will induce counterclockwise motion (this is based on the upper half of the flow going from left to right). Equations (7) and (9) uniquely determine the location and strength of the vortex from first principles. No additional calibration constants are used in the formulation.

By setting $\Delta z = \lambda_p$ predicted by Brennen's result, we presume that the linear theory provides the correct disturbance wavelength for the problem. The implications of this assumption are addressed in parametric studies in the following section. The λ_p observed in Hoyt and Taylor's case¹¹ is a function of the momentum thickness δ_2 , scaled by the parameter $\gamma = 0.175$. Presuming a high contraction ratio of the nozzle reduces the turbulence fluctuation, Hoyt and Taylor¹¹ assumed a laminarized flow over a flat plate and therefore they utilized the Blasius³¹ solution to approximate the momentum thickness.

$$\Gamma_v = \lambda_p = \left(\frac{2\pi}{0.175} \right) \delta_2. \quad (10)$$

Addition of the Biot–Savart law to the inviscid jet of BEM is expected to cause instability at the free surface that eventually forms a series of toroidal ligaments pinched off from the main body of the jet. Using Gauss' divergence theorem, we have transformed the surface integral to a line or contour integral and therefore have obtained the cross-sectional area of the ligaments as well as the centroids of the area. We have obtained the volume of the ligaments using the theorem of Pappus–Guldinus³³ which relates a volume of revolution to its generating cross-sectional area.

III. MODELING SECONDARY INSTABILITY

The nonlinear wavegrowth in high-speed liquid jets and in droplet splashing problems leads to a fully 3D surface that is beyond the capabilities of the axisymmetric model discussed in the prior section. Unfortunately, most of the data available for comparison of these complex flows are in the form of droplet size distributions. For this reason, we were motivated to incorporate a capability to assess the stability of liquid rings of fluid shed from the periphery of the axisymmetric jet simulated using the model. Certainly there are a large number of precedents for this approach in the atomization literature as analysts struggled with methodologies to permit predictions of drop sizes from linear results. Readers should be aware that the real phenomenon is more complex and that 3D behavior is evident prior to pinching of annular rings of fluid.

With these caveats in mind, we consider the annular ligaments as equivalent circular rings with the same liquid volume. Figures 3(a) and 3(b) highlight experimental and simulated ligaments near the point of pinch-off. The circulation

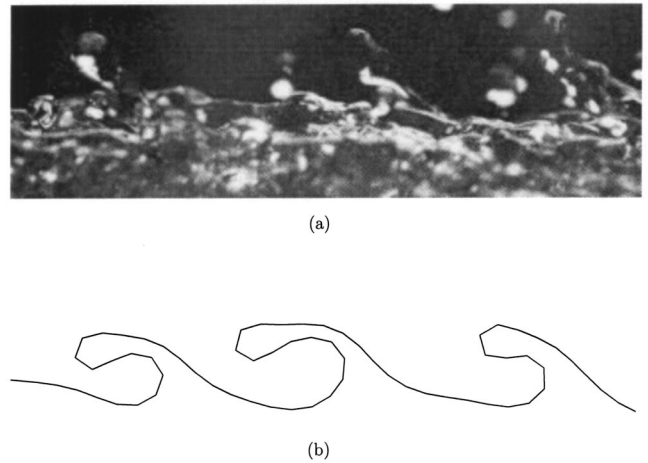


FIG. 3. (a) Closeup of the actual Hoyt and Taylor's water jet (Ref. 3). Printed under the permission of Journal of Fluid Mechanics. (b) The closeup of the model result for Hoyt and Taylor's water jet.

around the ring surface is computed at the point of pinch-off and is incorporated in the stability analysis. Droplets are assumed to form from secondary instability on these annular ligaments shed from the periphery of the jet. The linear stability analysis pertinent to this situation was due to Ponstein³⁴ (1959). Ponstein's work not only had extended Rayleigh's^{35,36} analysis to include gas-phase effects, but also considered column rotation (swirl) in an analysis published long before Sterling and Sleicher¹⁹ (1975), and even before Levich³⁷ (1962).

Ponstein had considered two cases: a rotating liquid column in gas phase and a rotating bubble (or gas) column in a liquid surrounding for the second case. A uniform liquid column in vacuum is well known by Rayleigh³⁵ who predicted the most dominant wavelength, $\lambda_s = 4.51d$. Rayleigh³⁶ also considered a uniform bubble column in liquid whose solution is

$$\omega^2 = \frac{\sigma}{\rho a^3} (1 - k^2 a^2) \xi \frac{K_1(\xi)}{K_0(\xi)}, \quad (11)$$

where $w = w_r + i w_i$ (i.e., w_r = growth rate, $i = \sqrt{-1}$, and w_i = frequency of oscillation), σ = surface tension of the liquid, ρ = liquid density, a = orifice radius, k = wave number = $2\pi/\lambda_s$ (i.e., λ_s = wavelength), $\xi = ka$, $K_1(\xi)$ and $K_0(\xi)$ are modified Bessel functions of the second kind. This equation predicts a most unstable wavelength, $\lambda_s = 6.48d$. For an axisymmetric rotating bubble column (based on $e^{\omega t}$), Ponstein gives the following result:

$$\omega^2 = \left[\frac{\sigma}{\rho a^3} (1 - k^2 a^2) - \left(\frac{\Gamma}{2\pi a^2} \right)^2 \right] \xi \frac{K_1(\xi)}{K_0(\xi)}, \quad (12)$$

where Γ is the circulation around the ring (or column) which can be estimated as $\Gamma = (2\pi a) V_\theta$ from Saffman.³⁸ Here V_θ is the tangential velocity of the ring surface. For a nonrotating case (i.e., $\Gamma = 0$), Eq. (12) recovers Rayleigh's result in Eq. (11). In this case, circulation has a stabilizing influence as indicated by the negative sign on the Γ term. The faster it rotates, the more stable the bubble ring is. The detailed dis-

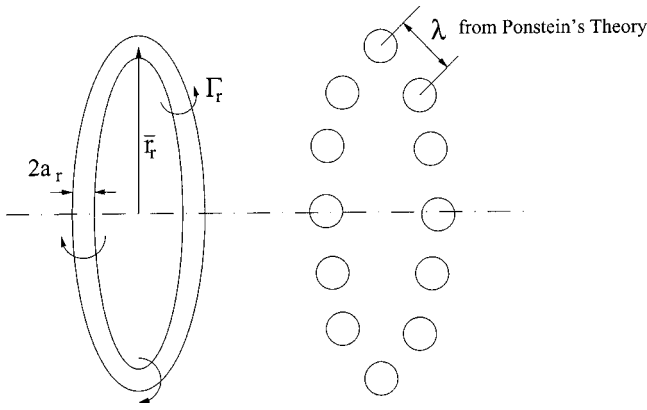


FIG. 4. Application of Ponstein's (Ref. 34) theory for the secondary instability of a pinch-off vortex-ring.

cussion of Eq. (12) is available in Lundgren and Mansour³⁹ where they had modeled the evolution of the bubble vortex-ring using the boundary integral method.

Ponstein gives the following result for the second case he had considered, a rotating liquid column in gas:

$$\omega^2 = \left[\frac{\sigma}{\rho a^3} (1 - k^2 a^2) + (1 - \epsilon) \left(\frac{\Gamma}{2\pi a^2} \right)^2 \right] \xi \frac{I_1(\xi)}{I_o(\xi)} + \epsilon U^2 k^2 \frac{I_1(\xi)}{I_o(\xi)} \frac{K_o(\xi)}{K_1(\xi)}. \quad (13)$$

If we consider the nonrotating (i.e., $\Gamma=0$) and nonaerodynamic effect (i.e., $U = \epsilon=0$), Rayleigh's result is recovered. Here, circulation has a destabilizing effect as indicated by the positive sign on the Γ term. The faster the column rotates, the more unstable it becomes. Increasing gas density ϵ serves to aid in stabilizing the column circulation term, but destabilizes the dominant aerodynamic (U^2) term. Considering the nonrotating case with an aerodynamic effect, Ponstein's equation (13) can be written as

$$\omega^2 = \frac{\sigma}{\rho a^3} (1 - k^2 a^2) \xi \frac{I_1(\xi)}{I_o(\xi)} + \epsilon U^2 k^2 \frac{I_1(\xi)}{I_o(\xi)} \frac{K_o(\xi)}{K_1(\xi)}. \quad (14)$$

For $\xi < 1.0$, it is known that $I_1(\xi)/I_o(\xi) \approx (\xi)/2$ (see Pearson⁴⁰). Applying this identity, Eq. (14) is rewritten as

TABLE I. Grid convergence test.

Δs	\bar{N}_D/ring	Stand. Dev.	SMD/d	\bar{u}_D	\bar{v}_D	\bar{U}_D
0.050	10.07	4.68	0.0995	0.608	0.442	0.752
0.040	10.87	8.71	0.0962	0.689	0.430	0.812
0.030	14.20	11.33	0.0841	0.790	0.479	0.924
0.020	12.46	8.46	0.0729	0.770	0.419	0.876
0.016	10.44	6.65	0.0623	0.779	0.404	0.877
0.012	10.87	6.44	0.0588	0.796	0.411	0.896

$$\omega^2 = \frac{\sigma}{2\rho a^3} (1 - k^2 a^2) (\xi)^2 + \epsilon \frac{U^2 (\xi)^3}{2a^2} \frac{K_o(\xi)}{K_1(\xi)}. \quad (15)$$

This result is exactly the same as the inviscid case of the dispersion relation derived by Sterling and Sleicher.¹⁹

We have considered the rotating case (i.e., $\Gamma \neq 0$) and nonaerodynamic effect (i.e., $U = \epsilon=0$) in order to model that the circulation around the rotating ring is the only source to cause the instability,

$$\omega^2 = \left[\frac{\sigma}{\rho a_r^3} (1 - k^2 a_r^2) + \left(\frac{\Gamma_r}{2\pi a_r^2} \right)^2 \right] (ka_r) \frac{I_1(ka_r)}{I_o(ka_r)}, \quad (16)$$

where a_r is the ring radius. If we choose the nondimensional parameters $k^* = ka_r$, $\Gamma_r^* = \Gamma_r / U a_r$, $\omega^* = \omega a / U$, and $We_r^* = \rho U^2 a_r / \sigma$, then the following expression is obtained:

$$\omega^2 = \left[\frac{1 - k^2}{We_r} + \left(\frac{\Gamma_r}{2\pi} \right)^2 \right] k \frac{I_1(k)}{I_o(k)}. \quad (17)$$

Note that nondimensional superscript, $()^*$, is eliminated to simplify notation. The expression accounts for capillary and circulation-based instabilities. This expression is solved to determine the $k = k_{\max}$ value attributed to the maximum growth rate, ω for a given ring geometry and circulation. Since Ponstein's analysis was conducted for a liquid column, we assume that the thickness of the ring-shaped ligaments is much less than the nozzle/jet radius (i.e., $a_r \ll a$). This assumption is confirmed from ligament sizes produced in the calculations. Figure 4 illustrates how Ponstein's equation is applied to the vortex ring (annular ligament) with circulation Γ_r . The circulation, Γ_r , takes into account the initial vorticity in the ring of fluid shed from the jet periphery. This

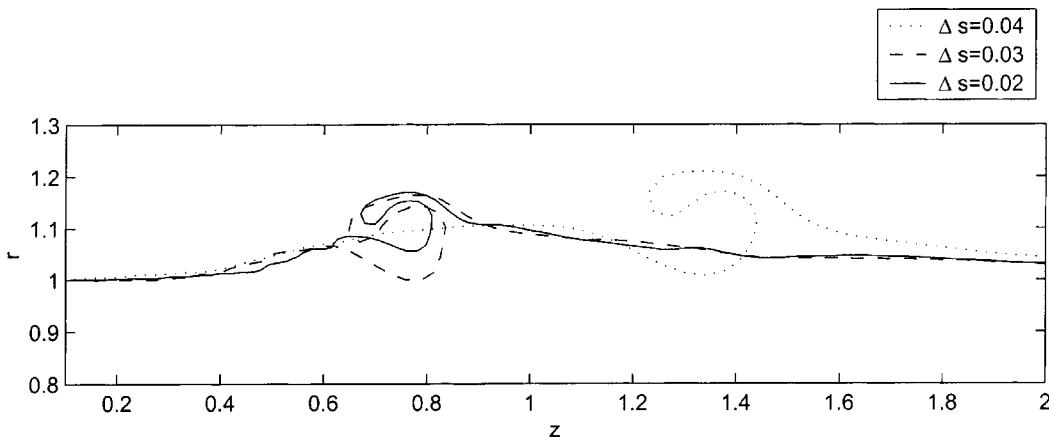
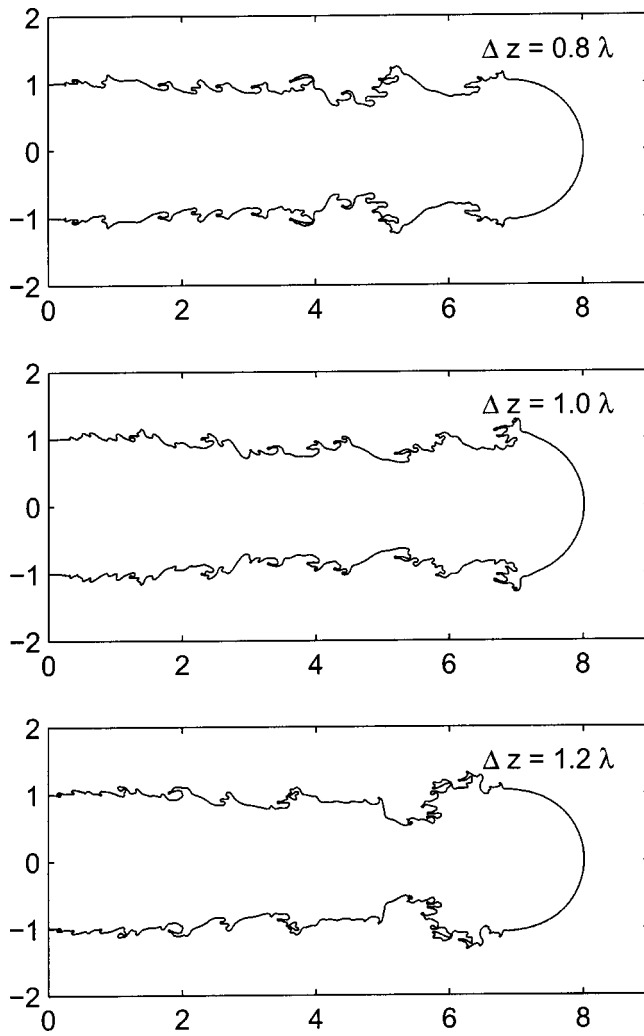


FIG. 5. Grid convergence study: Effect of nodal spacing, Δs , on surface shape.

FIG. 6. Effect of circulation level, Γ , on surface shape at $t=5.0$.

circulation is destabilizing for all wavelengths as indicated in Eq. (17); solution of the equation indicates that circulation leads to the formation of smaller droplets. Since each ring formed from the nonlinear evolution is unique in size and circulation, the overall effect of circulation is difficult to assess. The relation between the circulation and the number of droplets per ring is studied in Sec. V C below.

IV. MODEL VALIDATION AND CONVERGENCE STUDIES

Hoyt and Taylor's case is used for both the circulation of Eq. (9) and grid convergence study (i.e., $We=19057$, $\bar{r}=0.99$, and $\Gamma_v=0.139$). Let Δs represent the grid spacing for BEM nodes. While Hilbing²⁸ mentioned that $\Delta s=0.300$ is fine enough to resolve the low speed "Rayleigh's breakup" where waves are of length comparable to the orifice diameter, much finer grid resolution is required for high speed atomization where the wavelengths are comparable to the boundary layer thickness at the orifice exit. For this reason, the grid resolution for the present studies taxes the current computational capabilities of even advanced Linux-

TABLE II. Effect of the constant C of $\Delta z=C\lambda_p$ on SMD/d : Collected data up to $t=5.0$.

C	SMD/d	N_D	\bar{N}_D/ring	Stand. Dev.
0.8	0.0665	4142	10.31	7.4154
1.0	0.0655	5132	11.48	7.9848
1.2	0.0670	5700	11.54	7.7542

based compute clusters. In Fig. 5, it is shown that the axial location for the first ring pinch-off is reasonably insensitive to mesh spacing for $\Delta s < 0.030$.

However, grid function convergence studies indicate that a smaller mesh spacing is required for the accurate prediction of the droplet characteristics in the atomization regime. About 3000–5000 droplets were collected for each run for statistically reliable data; results for drop statistics are shown in Table I. The Sauter mean diameter (SMD) (drop whose diameter replicates the average surface area of drops in the population) is the most frequent measure used in the atomization field. Table I presents the number of drops per ring (\bar{N}_D), its SMD (nondimensionalized by orifice diameter), dimensionless drop axial/radial velocities at the pinching event (\bar{u}_D/\bar{v}_D), and drop speed at the pinching event (\bar{U}_D). A mesh spacing of $\Delta s=0.016$ was selected as a reasonable compromise between accuracy and runtime, i.e., the smallest mesh spacing led to excessive runtimes.

A study was conducted to assess the sensitivity of the surface evolution and droplet sizes to changes in the dimensionless circulation derived in Eq. (9). Figure 6 shows the liquid jet surface at various circulation levels [i.e., $C=0.8$, 1.0, and 1.2, where $\Delta z=C\lambda_p$ of Eq. (9)]. Results do show changes in the surface evolution as this important parameter is varied. Unfortunately, there are very few experimental observations save the Fig. 1 results that reinforce the $C=1$ value chosen for the study. The jet surface is slightly different at the different circulation level. However, Table II shows that SMD/d results are independent of the constant C . This indicates that the $\pm 20\%$ variation in Γ alone does not change the SMD/d results significantly. While this is certainly an area warranting additional study, we chose the $C=1$ value for the remaining studies due to its basis in linear theory and its success in explaining wavelengths observed in the Hoyt and Taylor studies.

There is no distinct time to stop the simulation since the jet can grow indefinitely depending on injection conditions. For the simulations conducted to date, the time required for the first pinching event is typically around $t \approx 1.7$. We found that collecting about 300–400 rings provides statistically re-

TABLE III. Effect of calculation time on droplet statistics.

t	SMD/d	N_D	\bar{N}_D/ring	Stand. Dev.
2.0	0.0628	88	7.97	3.329
3.0	0.0623	856	10.44	6.665
4.0	0.0635	2582	11.08	7.936
5.0	0.0655	5132	11.48	7.985
6.0	0.0664	7956	11.32	8.218

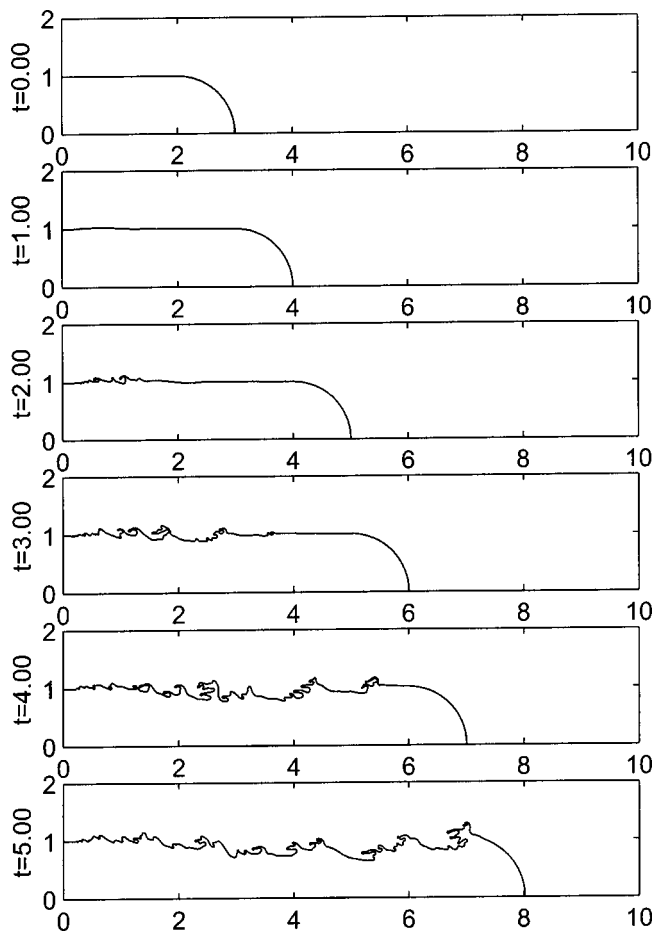


FIG. 7. Jet evolution for conditions consistent with Hoyt and Taylor's experiment (Ref. 3). Annular ligaments which have pinched off from the domain are not shown to improve clarity.

liable data. This would give roughly 3000–5000 droplets. Thus we typically stop our calculation at about $t \approx 5.0$. Table III shows that droplet statistics change little when $t > 4.0$.

V. RESULTS AND DISCUSSION

A. Simulation of Hoyt and Taylor's case

The complete simulation of Hoyt and Taylor's jet³ is shown in Fig. 7. The jet structure is initially assumed to be a simple cylinder with a hemispherical tip as shown in Fig. 2 and its evolution is simulated via time integration. A slight "swelling" is observed at $t = 1.0$ and a fluctuation of the jet surface is seen at $t > 2.0$. The velocities induced by the bound vortex are large enough to destabilize the jet surface resulting in primary atomization. It should be noted that most liquid ligaments pinching from the jet surface are in the "roll-up" motion in the counterclockwise direction while the mean velocity of the ligament is in the streamwise direction. Similar structures are noted in Fig. 3(a) in a closeup view of the Hoyt and Taylor experiment. The local surface from the simulation is included in Fig. 3(b). The mean velocity of most droplets are in the streamwise direction as droplet motions propagate along with the main jet stream, the most dominant convective source. The counterclockwise roll-up motion is strong evidence that the boundary layer instability

is the fundamental cause of the primary atomization in this experiment. The counterclockwise roll-up motion has not been observed if the jet were turbulent (see Fig. 1 of Wu *et al.*⁴¹) as this is presumed to lead to more complex three-dimensional modes.

It is interesting to note that the liquid core appears naturally as a consequence of the calculation. While the current model is based on the axisymmetric formulation (2D), the real instability is three-dimensional (3D). It is obvious that the loss of liquid mass of the model prediction is noticeably greater than that of actual 3D jet and, the liquid core forms more quickly than would be observed experimentally. This behavior is due in part to the fact that the model is inviscid and that atomization processes tend to be slowed by the presence of liquid viscosity. Prior work⁴² has shown similar behavior for BEM simulations; for low speed jets, viscosity has not been shown to play a significant role in droplet sizes. Presumably, viscous interactions become more important as smaller droplets are formed. More research is needed to quantify the role of liquid viscosity in determining droplet sizes for higher speed jets.

The modeling presumes that axisymmetric rings are instantaneously fractionated into droplets per the instability analysis of Ponstein. However, the experiment shows [see Fig. 1(a)] that the primary instability undergoes the transitional process to a 3D mode prior to the formation of droplets. Nevertheless, the model predicts droplet diameters (i.e., $d/10 - d/20$) which compare well with the experimental value of $d/15.5$ measured by Hoyt and Taylor.

B. Effect of Weber number for fully developed flow

We may consider a very long pipe laminar flow with constant diameter (i.e., $l/d \rightarrow \infty$) which would result in a fully-developed flow. In this case, the dimensionless velocity profile would remain the same for all speeds. The jet speed determines the regime of the jet instability because the momentum thickness is fixed (and therefore the dimensionless circulation is constant) for all speeds. In this case, the Weber number alone characterizes the stability of the free surface.

Eventually, the boundary layer instability disturbance will result in jet breakup regardless of the jet speed. If U is small that $We = 100$, the jet similar to Rayleigh's breakup is observed as shown in Fig. 8 (note: no atomization is observed for $t < 5.0$). If U increases up to $We = 1000$, the boundary layer instability is more prominent and numerous atomization events occur during the simulation. When $We = 10000$, the surface tension force is greatly reduced and therefore the atomization events occur at a higher rate; a similar pattern is observed for $We = 100000$.

In comparing these latter two cases in Fig. 8, similar wave patterns are observed on the surface, but the higher Weber number case experiences many more atomization events and loses more mass. The droplet statistics (Table IV) for these cases bear out this conclusion and the higher We case does show smaller droplets. In addition, greater dispersion in droplet sizes are apparent at the higher speed

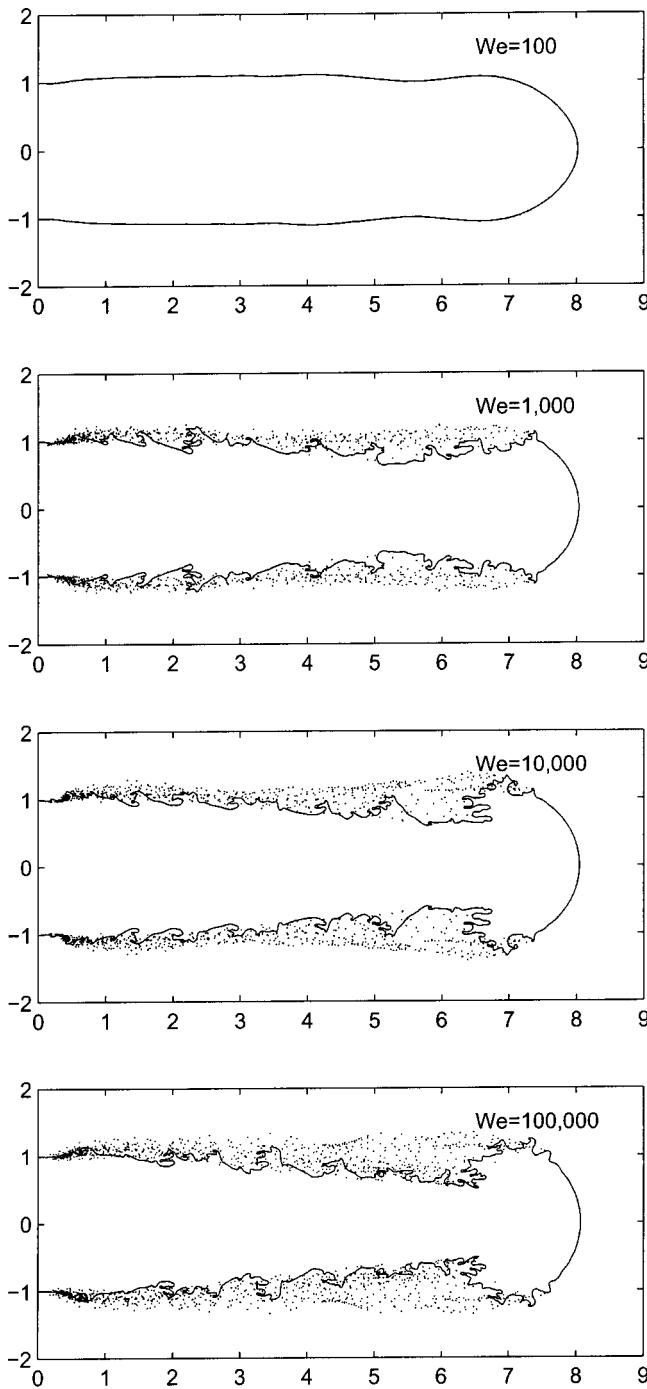


FIG. 8. Effect of Weber number on atomization of fully-developed jets.

conditions because a greater range of ligament sizes are pinched off in this case. Of course, secondary atomization could alter droplet distributions as well; the reader should keep in mind that these statistics are for primary atomization only.

TABLE IV. Effect of Weber number on drop statistics. Collected data up to $t=5.0$.

We	SMD/ d	N_D	\bar{N}_D/ring	Stand. Dev.
1 000	0.1034	1514	3.03	1.96
10 000	0.0733	5172	8.66	5.87
100 000	0.0507	18259	24.41	16.64

C. Effect of jet speed

In a fixed geometry orifice, changes in jet speed will influence both the internal boundary layer characteristics and the Weber number. Wu *et al.*⁴¹ provided both an empirical model and experimental observations for the SMD emphasizing the role of turbulence in the process. Their model is based on Kolmogorov length scale:⁴³

$$\frac{\text{SMD}}{\lambda_H} = \frac{133}{\text{We}_{l,\lambda_H}^{0.74}}. \quad (18)$$

Wu *et al.*⁴¹ introduced $\lambda_H = d/8$ for “radial integral length scales of the flow at the jet exit, based on measurements of Laufer for fully developed turbulent pipe flow cited Hinze.”⁴⁴ Using this length scale, Wu *et al.*⁴¹ were able to match their experimental data with the empirical formula below:

$$\frac{\text{SMD}}{d} = \frac{77.5}{\text{We}_{l,d}^{0.74}}, \quad \frac{\text{SMD}}{d} = \frac{46.4}{\text{We}^{0.74}}. \quad (19)$$

Note that $d=2a$. Here SMD is defined as

$$\text{SMD} = \frac{\sum_{i=1}^{N_D} D_i^3}{\sum_{i=1}^{N_D} D_i^2}, \quad (20)$$

where N_D is the number of droplet collected.

It is well known that the droplet size varies significantly within the atomization regime. Wu *et al.*⁴¹ reported the droplet size variation with U for turbulent water jet into air. Hoyt and Taylor’s experiment had been carried out for an orifice pressure drop $\Delta P < 60$ psi; no result with higher ΔP is reported.^{3,11,45} However, we hypothesized the increase in ΔP to 116 psi in order to project results for Hoyt and Taylor jet up to $U=40$ m/s. Figure 9 provides a comparison of these calculations with the experimental data of Wu and Faeth and Hoyt and Taylor. The figure also includes Brennen’s prediction based on boundary layer instability mechanisms. At the lower jet speeds near 20 m/s, Wu and Faeth’s data agree quite well with the measurements of Hoyt and Taylor. The calculations and Brennen’s theory also hold quite well in this region. The calculations provide SMD values similar to Brennen’s theory over the range of velocities studied thereby highlighting the importance of the boundary layer instability mechanism in laminar jets.

Our SMD results for Hoyt and Taylor’s case are approximately 90% of the primary instability waves as shown in Fig. 9 (i.e., $\text{SMD} = 0.9\lambda_p$). Our conclusion of 0.9 scaling constant is consistent with Hoyt and Taylor’s comparison; they too found the actual droplet size was a bit smaller than the theoretically predicted primary wavelength. However, this correlation is applicable for Hoyt and Taylor’s jet with the boundary layer driven spray only. The scaling constant may vary significantly depending on instability mechanism. For example, Wu *et al.*⁴⁶ showed that the scaling constant was 4.5 for the spray in the atomization regime for aerodynamically driven spray. Generally, the scaling constant is less than

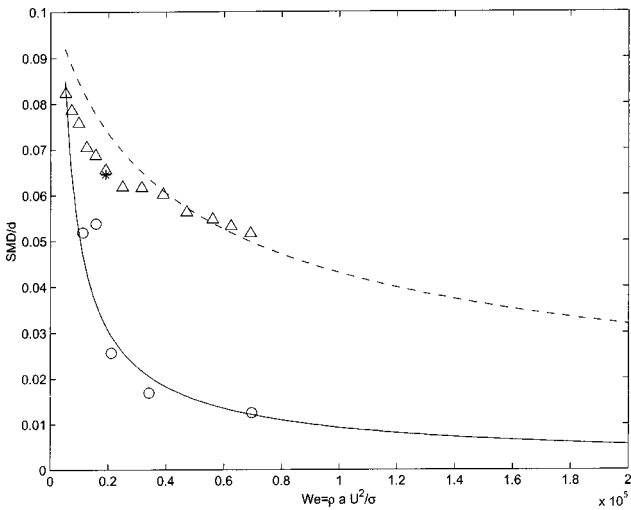


FIG. 9. Sauter mean diameter comparison at various jet speed for boundary layer instability jet and turbulent jet: $\rho=999 \text{ kg/m}^3$, $\sigma=0.073 \text{ kg/s}^2$, $d_{\text{Wu-Faeth}}=6.40 \text{ mm}$, $d_{\text{Hoyt-Taylor}}=6.35 \text{ mm}$; (dashed line) $\text{SMD}=\lambda_{p,B}$; (solid line) $\text{SMD}/d=46.4/\text{We}^{0.74}$ by Wu *et al.* (Ref. 41) for the turbulent jet; \circ , SMD from Wu (Ref. 41) experiment for the turbulent jet; $*$, SMD from Hoyt and Taylor experiment for the boundary layer instability laminar jet; Δ , SMD from the model prediction for the boundary layer instability laminar jet.

unity for turbulent jets. It should be noted that there is no direct proportionality as the ultimate drop size (which is determined from the secondary wavelength, λ_s) depends on the circulation, the size of the vortex ring, and the surface tension. For this reason, our “constant of proportionality” is continuously changing with the conditions pertaining to each individual ring. In Fig. 10, the number of droplets as a function of circulation for the Hoyt and Taylor’s case is shown. The relation shows a parabolic behavior with the number of droplets growing as the square of Γ_r . Significant scatter is observed due to the range of ring sizes and initial conditions brought about by the nonlinear jet evolution.

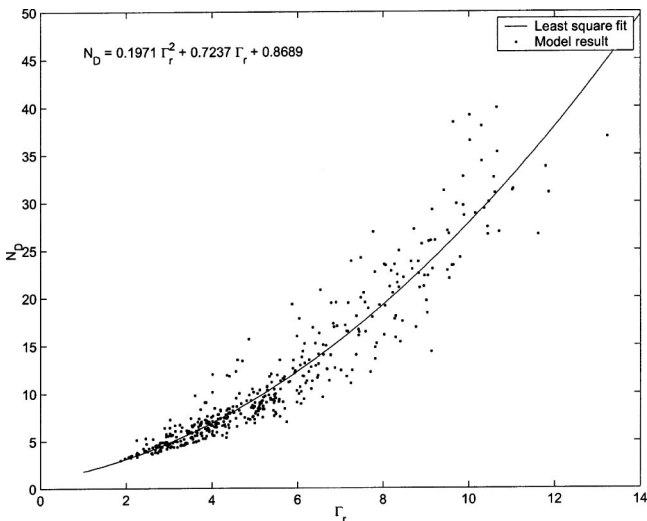


FIG. 10. Prediction of circumferential wave number (or number of droplet) due to circulation around the rotating ring pinched-off from the main liquid stream.

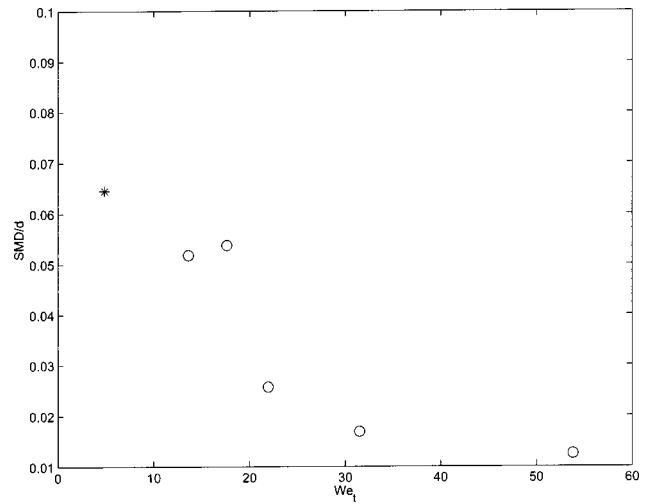


FIG. 11. The same case as Fig. 9, where $\text{We}_t=(\rho U^2 \delta_2)/(\sigma \sqrt{\text{Re}_{\delta_2}})$. While the Blasius solution is used to estimate δ_2 for the Hoyt and Taylor jet (Ref. 11), δ_2 for the Wu *et al.* data (Ref. 41) is analytically calculated using the power-law (Ref. 44) fully developed turbulent velocity profile with $n=7$.

However, Wu and Faeth data show a significant departure to much smaller SMD values as jet speed is increased. In fact, there is a very sharp drop in SMD near $U=20 \text{ m/s}$ with the remaining data showing a more modest change with increased speed. This behavior could possibly be attributed to a turbulence transition; or the role of turbulence becoming an important factor in this region. In later work⁴⁷ Faeth’s group reports a transition to turbulence between 16 and 26 m/s; in the range where the dramatic changes in drop sizes occur. Turbulent eddies could be interacting with the mean vorticity produced in the boundary layer to effect the wavelengths of instability and hence the drop sizes. To investigate this behavior, consider the radial velocity induced by a vortex ring. Using the methodology described in Eq. (10), the induced velocity (nondimensionalized by the mean flow velocity, U), should scale as

$$v_{rv}^* \propto \frac{\Gamma_v}{\delta_2} = \frac{2\pi}{0.175}, \tag{21}$$

where $v_{rv}^*=v_{rv}/U$. In contrast, the dimensionless radial velocity induced by turbulent eddies is known to be related to the Reynolds number based on the momentum thickness:

$$v_t^* \propto \frac{1}{\text{Re}_{\delta_2}^{1/4}}, \tag{22}$$

where $v_t^*=v_t/U$. In comparing these two velocities, other researchers have noted the diminishing influence of turbulent fluctuations as jet velocity is increased. However, another way to think about this issue is that the turbulence can be a dominant force in the growth of non-axisymmetric disturbances. In these circumferential modes, the bulk vorticity imparted from the axisymmetric boundary layer plays at most a minor role and the sole forces imparted to the surface result from interactions with turbulent eddies and surface tension. Define a Weber number for this turbulence interaction:

$$\text{We}_t = \frac{\rho(Uv_t^*)^2 \delta_2}{\sigma}. \tag{23}$$

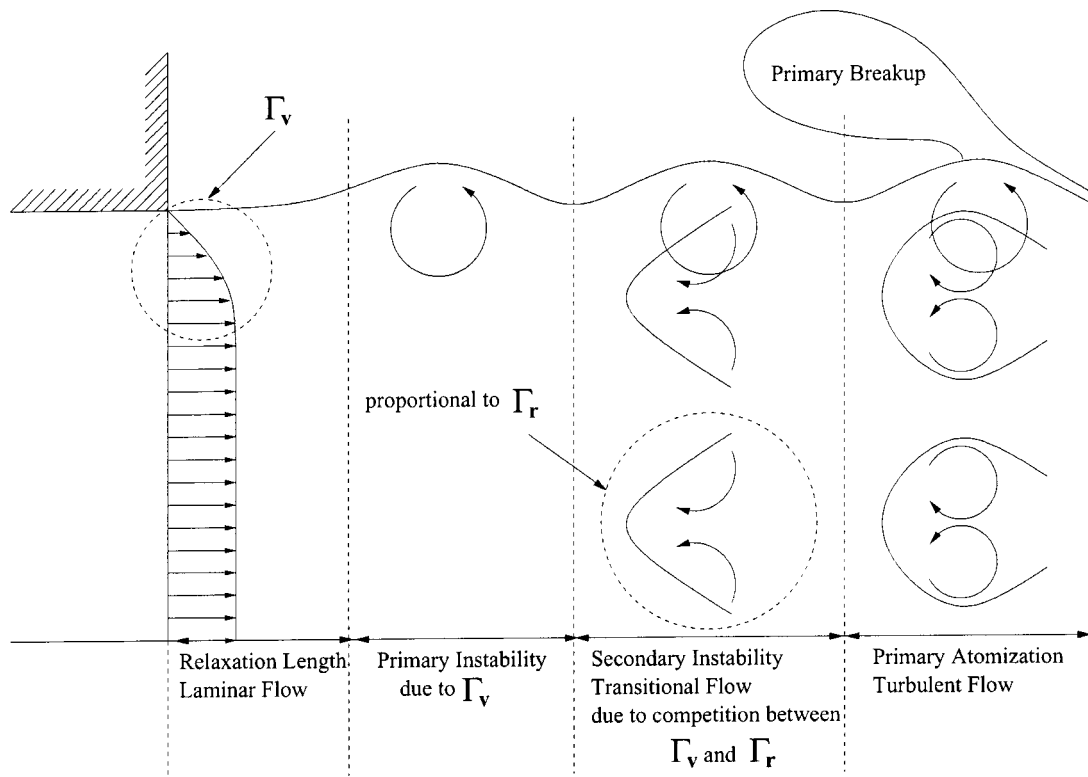


FIG. 12. Transformation of the primary waves into secondary waves due to the competition between the surface tension force against the vorticity arising in azimuthal direction.

Assuming the constant of proportionality in the expression for v_t^* , Eq. (22), is unity this turbulent Weber number becomes

$$We_t = \frac{\rho U^2 \delta_2}{\sigma \sqrt{Re_{\delta_2}}} \tag{24}$$

If $We_t \gg 1$, we expect the dynamic pressure induced by turbulent eddies to dominate over surface tension forces; if $We_t \ll 1$ we expect the opposite effect. However, one must keep in mind that the scaling coefficient for the turbulent velocity is in general not known *a priori*.

Figure 11 depicts the Wu and Faeth data plotted on this basis, showing an abrupt change in droplet sizes near a threshold of $We_t \approx 20$. Certainly, it would be beneficial to obtain additional data to confirm this threshold; in particular experiments that quantify turbulence intensity levels would be most beneficial in providing a better quantitative assessment of We_t . At the moderate speeds of the Hoyt and Taylor jet¹¹ turbulence plays a minimal role on the initial instability. The inviscid instability is the fundamental linear mechanism, while turbulence can affect the nonlinear evolution. If turbulence effects were greater, the boundary layer waves near nozzle exit would have not been visible; the inviscid instability would have already caused the turbulence before the flow exits the orifice. However, the turbulence in Hoyt and Taylor’s jet does eventually appear subsequent to the transitional flow (see Fig. 1). While the primary boundary layer-

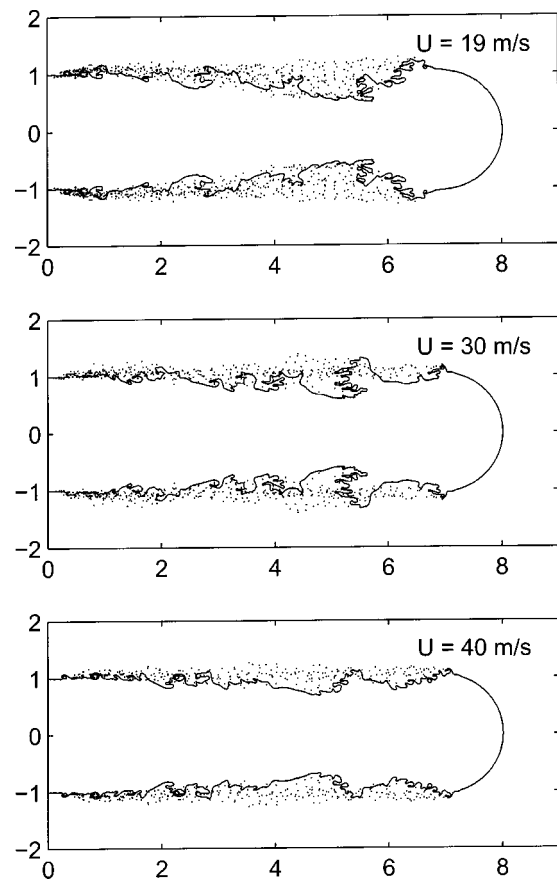


FIG. 13. Effect of jet speed on jet surface structure of Hoyt–Taylor’s jet.

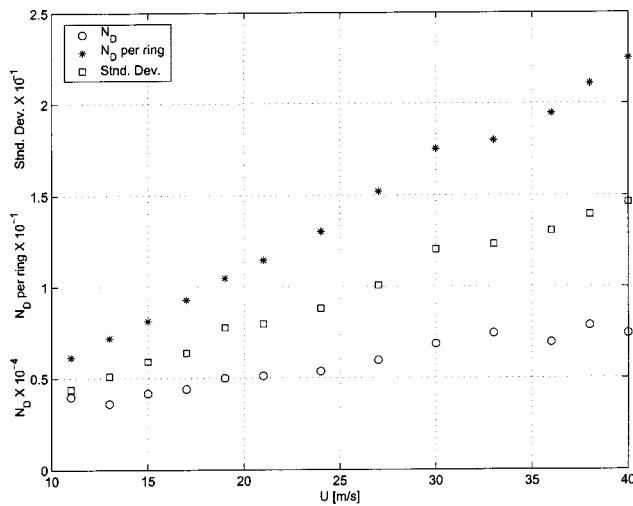


FIG. 14. Effect of jet speed on drop statistics.

generated waves propagate axially, the axisymmetric waves fragment into the number of droplets due to the competition between the surface tension force and the vorticity transformed (or propagated) into the azimuthal direction as depicted in Fig. 12. This three-dimensional phenomenon indicates that the substantially reduced turbulence fluctuation in the converging nozzle eventually appears and plays an important role in causing the nonlinear evolution azimuthally; “the secondary instability for primary atomization.”

Figure 13 provides a comparison of computed jet surfaces for three different jet speeds. We regret that we cannot consider a larger range of speeds in that computational limits preclude the resolution required for speeds greater than 40 m/s. The higher speed jets are subject to a larger number of atomization events, but the total ejected mass is actually larger for the lower speed case as indicated in the figure. The larger wavelength instabilities at the lower jet speeds leads to greater overall deformations of the jet surface and greater penetration into the “core” region of the jet. The droplet and

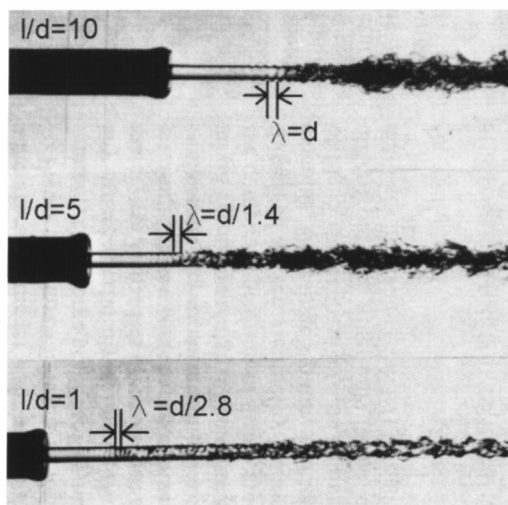
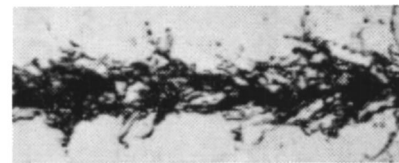
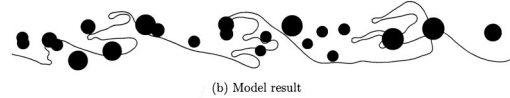


FIG. 15. McCarthy and Molloy’s experiment (Ref. 50) for $l/d=10, 5,$ and 1 : The most dominant wavelength is highlighted for each case. Printed under the permission of Elsevier Science.



(a) Experiment



(b) Model result

FIG. 16. Liquid: 60% glycerol and 40% water by weight, $\rho=103 \text{ kg/m}^3$, $\mu=11 \text{ cP}$, $\sigma=0.0669 \text{ kg/s}^2$, $U=20 \text{ m/s}$, $d=2.54 \text{ mm}$, $We=781$, $Re=4750$. Comparison between experiment (Ref. 50) and model results. The black circles represent the location and the relative size of the pinched-off droplets. Printed under the permission of Elsevier Science.

ring formation statistics for the three cases shown in Fig. 13 are summarized in Fig. 14. The total number of droplets, N_D , number of drops per ring, N_D/ring , and its standard deviation all tend to increase with increasing U . These results are consistent with the Weber number trends shown in the last section as at higher Weber number a larger range of wavelengths are unstable so that greater variability in drop sizes is possible.

D. Effect of orifice length

For a fixed pressure drop, changing the orifice length (l/d in dimensionless sense) is essentially the same as changing the boundary layer thickness. The effect of l/d for the jet breakup has been investigated by many researchers.^{9,19,48–50} For the Rayleigh and first wind-induced regime ($We_g = \rho_g U^2 d / \sigma < 2.55$), Sterling–Sleicher’s experimental data shows that the breakup (or jet) length, L , decreases with increasing nozzle length, l . This indicates that the velocity profile with thicker boundary layer breaks up faster due to larger wavelength instabilities convected into the free surface.

For the second wind-induced regime, McCarthy and Molloy⁵⁰ also investigated the effect of l/d on the atomization mechanism as shown in Fig. 15. The jet surface is shown up to 70 diameters downstream while jet speed remains constant. A 60% glycerol and 40% water mixture was used, resulting in $We=781$, $Re_d=4750$, and $We_g=18.7$ for

TABLE V. Summary for McCarthy and Molloy’s experiment (Ref. 50). (Note: Blasius solution is used for δ_1 and δ_2 estimation.)

l/d	Re_x^a	δ_1/d	δ_2/d	Re_{δ_2}	f^b (Hz)	λ_p^c	$\lambda_{p,exp}$
1	4748	1/40.04	1/103.8	46	22758	d/2.9	d/2.8
5	23738	1/17.90	1/46.41	102	10178	d/1.3	d/1.4
10	47477	1/12.66	1/32.82	145	7197	1.1 d	1.0 d

^aWhere $Re_x = Ux/\nu$.

^{b,c} $f = \gamma U / 2\pi \delta_2$ and $\lambda_p \approx U/f$.

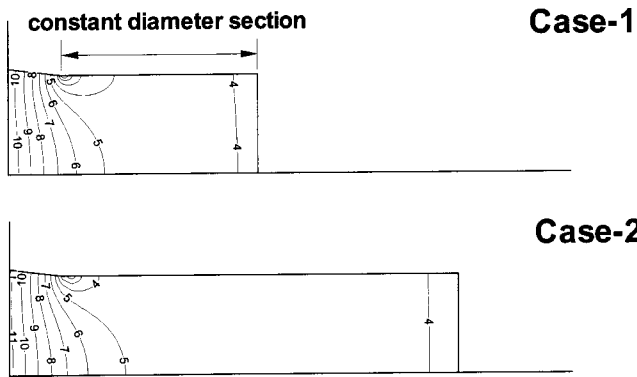


FIG. 17. Pressure distribution and assumed nozzle geometry (Ref. 11) for nozzle length studies. Note that “Case-3” is the fully-developed flow (i.e., $l/d = \infty$).

$l/d = 0, 1, 5,$ and 10 . These conditions place the flow in the lower part of the second wind-induced regime. Results in Fig. 15 show a wrinkled jet for the low $l/d = 1$, with the higher l/d cases showing atomization. The wavelengths of the instabilities increase with l/d as does the thickness of the boundary layer.

In Fig. 16(a), the backward-leaning wave structures also observed by Hoyt and Taylor are prominent. A calculation was performed for this case and the results are shown in Fig. 16(b) showing similar behavior. Even though this case lies in the second wind-induced regime in which gas pressure variations on the surface are known to play a role, it appears that

the boundary layer instabilities are dominant since the model does not include the influence of gas pressure. This observation is important in that the role of the boundary layer is often neglected by researchers in favor of concentrating on the influence of gas properties. Vorticity convected into the free surface represents a large nonlinear disturbance for high speed jets.

McCarthy and Molloy’s experiment is summarized in Table V, which shows an excellent agreement between the wavelength predicted by Brennen’s boundary layer analysis and the experimental results. This comparison provides further evidence of the importance of the boundary layer instability mechanism.

The model was used to simulate the effects of changes in orifice length by considering $l/d = 1, 2,$ and ∞ using the flow conditions consistent with Hoyt and Taylor’s experiment as shown in Fig. 17. Only the boundary layer thickness changes while everything else remains constant (i.e., $We = 19057$ and $Re_d = Ud/\nu = 1.12 \times 10^5$). Figure 18 shows the computed jet surfaces at two instances in time. It is evident that the larger wave instabilities associated with the higher l/d nozzle leads to significantly more atomization and erosion of the liquid core. Hiroyasu *et al.*⁴⁸ (i.e., water jet into air) measured decreases in intact core length with increased l/d ; a result in agreement with the trends shown in our analysis. Figure 19 highlights the ring pinching events for each of the three cases studied. It is evident that more atomization (ring pinching) events tend to occur with an increased l/d . Table VI summarizes drop statistics from the three calculations. Here, there

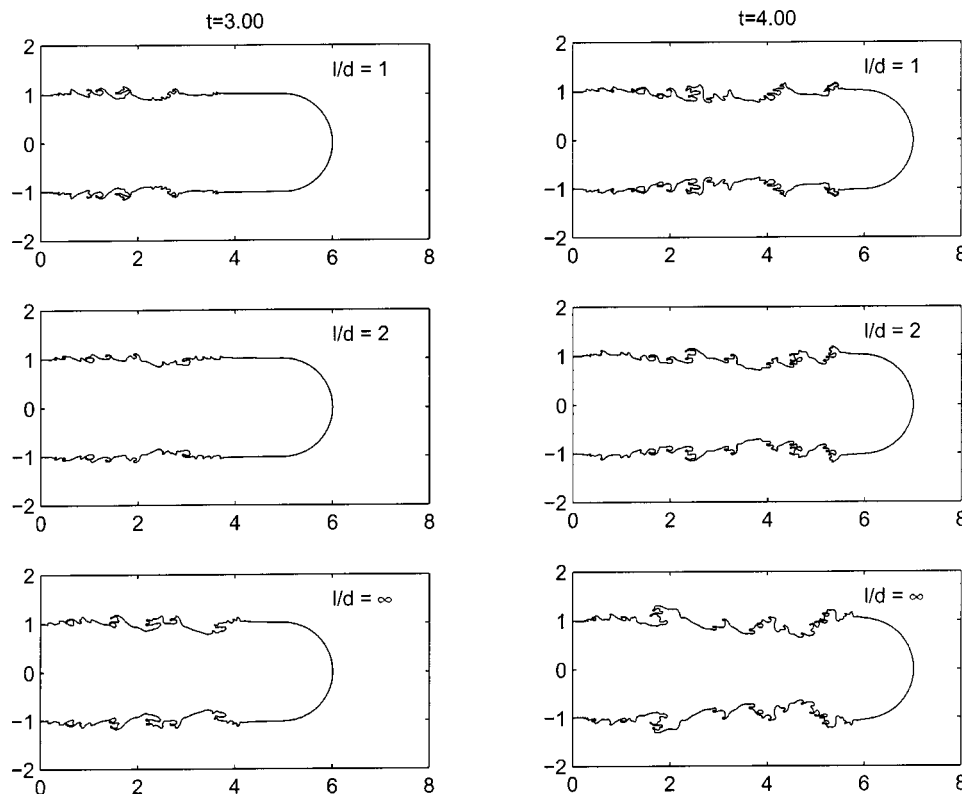


FIG. 18. Jet surface profiles at different times for three different l/d values.

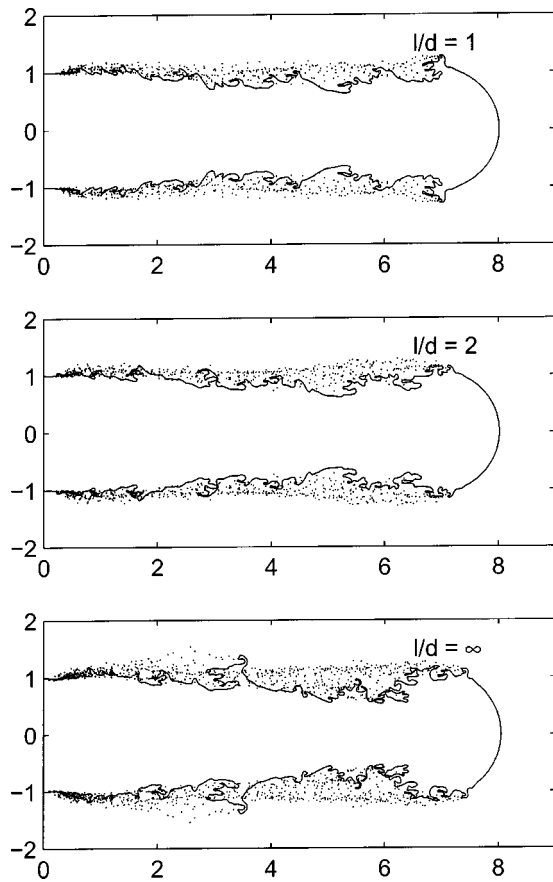


FIG. 19. Jet surface shape and atomization locations at $t=5$ for three different orifice l/d values.

appears to be no major trend in drop sizes with l/d . Similar conclusions were noted by previous researchers.^{48,49}

VI. CONCLUSIONS

An axisymmetric model based on a boundary element formulation is used to simulate nonlinear primary atomization processes attributable to vorticity convected from the orifice boundary layer to the free surface. A ring vortex, whose strength and location are uniquely determined by the boundary layer characteristics at the orifice exit, is used to account for vorticity convected toward the free surface. A linear instability analysis due to Ponstein is used to predict the fractionization of rings of fluid shed from the periphery of the jet thereby providing a mechanism to predict droplet size distributions from first principles without the aid of empirical constants.

The model shows good agreement with surface characteristics and droplet sizes for laminar jets; turbulence appears to alter the three-dimensional evolution and reduce droplet

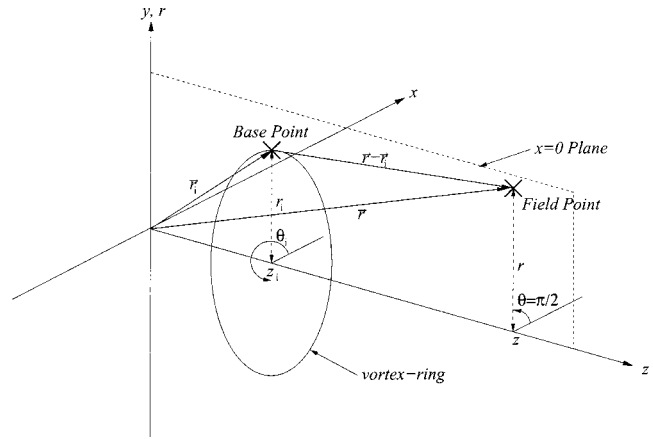


FIG. 20. A schematic of vortex-ring geometry for computing induced velocities at arbitrary field points.

sizes from those predicted with the model. At low Weber numbers, wrinkled jets are simulated and higher Weber numbers lead to smaller drops and greater dispersions in drop statistics as observed experimentally. The boundary layer thickness at the orifice exit plane is shown to have significant impact on the results with thicker boundary layers (consistent with longer orifice passages) leading to increased atomization with only minor changes in droplet sizes.

ACKNOWLEDGMENTS

The authors gratefully acknowledge the support of Dr. Mitat Birkan and the AFOSR under Grant No. F49620-99-1-0092. The authors also wish to acknowledge useful discussions with Professor Greg Blaisdell of Purdue University.

APPENDIX

Figure 20 highlights the applicable geometry required to compute velocities at a “field point,” z, r subject to a ring vortex located at a point z_i, r_i . Traditionally,⁵¹ the velocities induced from this flow are computed from the stream function^{17,25,51,52} ψ :

$$\psi(z, r) = \frac{\Gamma}{2\pi} \sqrt{r_i r} \left[\left(\frac{2}{\sqrt{m}} - \sqrt{m} \right) K(m) - \frac{2}{\sqrt{m}} E(m) \right], \tag{A1}$$

where $m = 4rr_i/a$ and $a = (r+r_i)^2 + (z-z_i)^2$. Here, the strength of the vortex is Γ and the functions $K(m)$ and $E(m)$ represent complete elliptic integrals of the first and second kind, respectively,

TABLE VI. Model predictions for different boundary layer. Collected data up to $t=5.0$.

Case	l/d	δ_1/d	δ_2/d	SMD/d	N_D	\bar{u}_D	\bar{v}_D	\bar{N}_D/ring	Stand. Dev.
1	1.0	1/200	1/518	1/15.27	5132	0.809	0.424	11.48	7.98
2	2.0	1/141	1/367	1/15.19	5879	0.817	0.428	11.59	8.25
3	∞	1/6	1/24	1/14.81	8133	0.811	0.457	11.69	8.40

$$K(m) = \int_0^{\pi/2} \frac{1}{\sqrt{1-m \sin^2 \phi}} d\phi,$$

$$E(m) = \int_0^{\pi/2} \sqrt{1-m \sin^2 \phi} d\phi. \quad (\text{A2})$$

The velocities can be determined in a standard fashion by differentiating ψ :

$$u_z = \frac{1}{r} \frac{\partial \psi}{\partial r}, \quad u_r = -\frac{1}{r} \frac{\partial \psi}{\partial z}. \quad (\text{A3})$$

The classic texts from Lamb,⁵² Batchelor,⁵¹ and Saffman¹⁷ do not carry this analysis beyond this point. Ramsey²⁵ presents approximate results for only the axial velocity, u_z . The complete solution is presented as follows:

$$\frac{\partial \psi}{\partial z} = \left(\frac{\Gamma}{4\pi} \frac{z-z_i}{\sqrt{a}} \right) \left[c_1 K(m) + c_2 \frac{dK(m)}{dm} + c_3 \frac{d^2 K(m)}{dm^2} \right], \quad (\text{A4})$$

$$\frac{\partial \psi}{\partial r} = \left(\frac{\Gamma}{4\pi} \frac{r+r_i}{\sqrt{a}} \right) \left[d_1 K(m) + d_2 \frac{dK(m)}{dm} + d_3 \frac{d^2 K(m)}{dm^2} \right], \quad (\text{A5})$$

with the following coefficients $c_1 - c_3$ and $d_1 - d_3$:

$$c_1 = m + \frac{4B}{a}, \quad c_2 = 4m(m-1) + \frac{4B}{a}(9m-4),$$

$$c_3 = \frac{16B}{a}m(m-1), \quad (\text{A6})$$

$$d_1 = m + \rho, \quad d_2 = 4m(m-1) + (9m-4)\rho,$$

$$d_3 = 4m(m-1)\rho, \quad (\text{A7})$$

where

$$\rho = \frac{4r_i}{(r+r_i)} + \frac{4B}{a}, \quad B = -2rr_i. \quad (\text{A8})$$

At the centerline, the radial location of the field point is zero which leads to a singularity in Eq. (A3). In this case, however, the integrals of the Biot–Savart law can be integrated analytically the result of which is

$$u_z = \frac{\Gamma}{2} \frac{r_i^2}{[r_i^2 + (z-z_i)^2]^{3/2}} \quad u_r = 0, \quad (\text{A9})$$

which agrees with the prior results of Robertson⁵³ and Duncan *et al.*²⁴

- ¹K. J. DeJuhász, "Dispersion of sprays in solid injection oil engines," *Trans. ASME* **53**, 65 (1931).
²W. Bergwerk, "Flow patterns in diesel nozzle spray holes," *Proc. Inst. Mech. Eng.* **173**, 655 (1959).
³J. W. Hoyt and J. J. Taylor, "Waves on water jets," *J. Fluid Mech.* **83**, 119 (1977).
⁴H. Schlichting, *Boundary Layer Theory* (McGraw–Hill, New York, 1979), pp. 461–463.
⁵R. L. Panton, *Incompressible Flow*, 2nd ed. (Wiley, New York, 1996), pp. 460–470, 718–727, 739–741.
⁶J. H. Rupe, "On the dynamic characteristics of free liquid jets and a partial

- correlation with orifice geometry," NASA JPL Technical Report No. 32-207 (1962).
⁷V. Y. Shkadov, "Wave formation on surface of viscous liquid due to tangential stress," *Fluid Dyn.* **5**, 473 (1970).
⁸J. M. Gordillo, M. Perez-Saborid, and A. M. Ganan-Calvo, "Linear stability of co-flowing liquid-gas jets," *J. Fluid Mech.* **448**, 23 (2001).
⁹R. D. Reitz and F. V. Bracco, "Mechanism of atomization of a liquid jet," *Phys. Fluids* **25**, 1730 (1982).
¹⁰P. K. Wu and G. M. Faeth, "Aerodynamic effects on primary breakup of turbulent liquids," *Atomization Sprays* **3**, 265 (1993).
¹¹J. W. Hoyt and J. J. Taylor, "Turbulence structure in a water jet discharging in air," *Phys. Fluids* **20**, S253 (1977).
¹²C. Brennen, "Cavity surface wave patterns and general appearance," *J. Fluid Mech.* **44**, 33 (1970).
¹³S. S. Yoon and S. D. Heister, "Categorizing linear theories for atomizing round jets," *Atomization Sprays* (to be published).
¹⁴A. J. Chorin, "Numerical study of slightly viscous flow," *J. Fluid Mech.* **57**, 785 (1973).
¹⁵A. J. Chorin and P. S. Bernard, "Discretization of a vortex sheet," *J. Comput. Phys.* **13**, 423 (1973).
¹⁶A. J. Chorin, "Vortex sheet approximation of boundary layers," *J. Comput. Phys.* **27**, 428 (1978).
¹⁷P. G. Saffman, *Vortex Dynamics* (Cambridge University Press, New York, 1992), pp. 22, 192–195.
¹⁸S. S. Yoon and S. D. Heister, "A fully nonlinear model for atomization of high-speed jets," *Eng. Anal. Boundary Elements* (to be published).
¹⁹A. M. Sterling and C. A. Sleicher, "The instability of capillary jets," *J. Fluid Mech.* **68**, 477 (1975).
²⁰J. A. Liggett and P. L.-F. Liu, *The Boundary Integral Equation Method for Porous Media Flow* (George Allen and Unwin, New York, 1983).
²¹S. D. Heister, "Boundary element methods for two-fluid free surface flows," *Eng. Anal. Boundary Elem.* **19**, 309 (1997).
²²I. F. Murray and S. D. Heister, "On a droplet's response to acoustic excitation," *Int. J. Multiphase Flow* **25**, 531 (1999).
²³S. S. Yoon, S. D. Heister, J. T. Epperson, and P. E. Sojka, "Modeling multijet mode electrostatic atomization using boundary element methods," *J. Electrostat.* **50**, 91 (2001).
²⁴W. J. Duncan, A. S. Thom, and A. D. Young, *An Elementary Treatise on the Mechanics of Fluids* (Edward Arnold, London, 1960), pp. 93–94.
²⁵A. S. Ramsey, *A Treatise on Hydromechanics* (Bell and Sons, London, 1920), pp. 241–244.
²⁶K. Karamcheti, *Principles of Ideal-Fluid Aerodynamics* (Wiley, New York, 1966), pp. 526–530, 599.
²⁷I. G. Currie, *Fundamental Mechanics of Fluids*, 2nd ed. (McGraw–Hill, New York, 1993), pp. 172–174.
²⁸J. H. Hilbing, "Nonlinear modeling of atomization processes," Ph.D. thesis, Purdue University (1996).
²⁹E. Kreyszig, *Advanced Engineering Mathematics* (Wiley, New York, 1993), pp. 949–956.
³⁰M. S. Longuet-Higgins and E. D. Cokelet, "The deformation of steep surface waves on water," *Proc. R. Soc. London, Ser. A* **350**, 1 (1976).
³¹F. M. White, *Viscous Fluid Flow*, 2nd ed. (McGraw–Hill, New York, 1991), pp. 235, 269, 358.
³²B. Thwaites, *Incompressible Aerodynamics* (Dover, New York, 1960), pp. 30–31.
³³I. H. Shames, *Engineering Mechanics* (Prentice–Hall, Englewood Cliffs, NJ, 1993), pp. 306–308.
³⁴J. Ponstein, "Instability of rotating cylindrical jets," *Appl. Sci. Res., Sect. A* **8**, 425 (1959).
³⁵W. S. Rayleigh, "On the instability of jets," *Proc. London Math. Soc.* **10**, 71 (1878).
³⁶W. S. Rayleigh, "On the instability of cylindrical fluid surfaces," *Philos. Mag.* **34**, 177 (1892).
³⁷V. G. Levich, *Physicochemical Hydrodynamics* (Prentice–Hall, Englewood Cliffs, NJ, 1962), pp. 639–646.
³⁸P. G. Saffman, "The number of waves on unstable vortex rings," *J. Fluid Mech.* **84**, 625 (1978).
³⁹T. T. Lundgren and N. N. Mansour, "Vortex ring bubbles," *J. Fluid Mech.* **224**, 177 (1991).
⁴⁰C. E. Pearson, *Handbook of Applied Mathematics* (Van Nostrand Reinhold, New York, 1974), pp. 349–350, 361.
⁴¹P. K. Wu, L. K. Tseng, and G. M. Faeth, "Primary breakup in gas/liquid mixing layers for turbulent liquids," *Atomization Sprays* **2**, 295 (1992).
⁴²S. S. Yoon, S. D. Heister, J. T. Epperson, and P. E. Sojka, "Modeling

- multijet mode electrostatic atomization using boundary element methods,” *J. Electrostat.* **50**, 91 (2001).
- ⁴³H. Tennekes and J. L. Lumley, *A First Course in Turbulence* (MIT Press, Cambridge, 1975), pp. 248–286.
- ⁴⁴J. O. Hinze, *Turbulence*, 2nd ed. (McGraw–Hill, New York, 1975), pp. 625–631, 427.
- ⁴⁵J. W. Hoyt and J. J. Taylor, “Effect of nozzle boundary layer on water jets discharging in air,” in *Jets and Cavities—International Symposium*, ASME, Miami Beach, Florida, November 17–22, 1985, pp. 93–100.
- ⁴⁶K. J. Wu, R. D. Reitz, and F. V. Bracco, “Measurements of drop size at the spray edge near the nozzle in atomizing liquid jets,” *Phys. Fluids* **29**, 941 (1986).
- ⁴⁷P. K. Wu, R. F. Miranda, and G. M. Faeth, “Effects of initial flow conditions on primary breakup of nonturbulent and turbulent liquid jets,” in *32th Aerospace Sciences Meeting and Exhibit*, AIAA 94-0561 Reno, NV, 1994.
- ⁴⁸H. Hiroyasu, M. Shimizu, and M. Arai, “The breakup of high speed jet in a high pressure gaseous atmosphere,” in *Proceedings of the 2nd International Conference on Liquid Atomization and Spray Systems*, ICLASS, Madison, Wisconsin, 1982, pp. 69–74.
- ⁴⁹M. Arai, M. Shimizu, and H. Hiroyasu, “Breakup length and spray angle of high speed jet,” in *Proceedings of the 3rd International Conference on Liquid Atomization and Spray Systems*, ICLASS, London, United Kingdom, 1985, pp. 1B/4/1–10.
- ⁵⁰M. J. McCarthy and N. A. Molloy, “Review of stability of liquid jets and the influence of nozzle design,” *Chem. Eng. J.* **7**, 1 (1974).
- ⁵¹G. K. Batchelor, *An Introduction to Fluid Dynamics* (Cambridge University Press, New York, 1967), pp. 511–517, 521–526.
- ⁵²H. Lamb, *Hydrodynamics* (Dover, New York, 1879), pp. 236–239.
- ⁵³J. Robertson, *Hydrodynamics in Theory and Application* (Prentice–Hall, Englewood Cliffs, NJ, 1965), pp. 128–132.